Sustainable Energy & Fuels

ROYAL SOCIETY OF CHEMISTRY

COMMUNICATION

View Article Online
View Journal | View Issue

Cite this: *Sustainable Energy Fuels*, 2024, **8**, 1405

Received 21st December 2023
Accepted 24th February 2024

DOI: 10.1039/d3se01680c

rsc.li/sustainable-energy

Improved photocatalytic carbon dioxide reduction over Bi-doped CeO_2 by strain engineering†

Ang Tian,[a] Ziyu Mei,[b] Luyuan Wang,[b] Guangliang Liu,[c] Zhiguo Liu,[d] Guangming Kong,[d] Wenjun Tang*[e] and Chuangwei Liu *[b]

Room-temperature photocatalytic carbon dioxide reduction reaction (CRR) is an essential method for reducing carbon footprint and achieving valuable fuels. The key challenge to accelerating the process is enhancing the catalytic rate and product selectivity. Herein, we investigate the conversion of carbon dioxide to formic acid on Bi-doped CeO_2 in the presence of tensile and compressive strain by using density functional theory corrected for on-site coulombic interactions. As demonstrated, the dopant atom not only benefits the oxygen vacancy formed, but also transfers some electrons to the Ti^{3+} site, which is the main catalytic site for the CRR. The promising model has excellent product selectivity, offering the best catalytic performance for formic acid (ΔG_{max} = 0.64 eV). Moreover, the catalytic performance is further improved by the compressive strain. The work provides novel insights into designing environment-friendly and low-cost CeO_2-based photocatalysts for carbon reduction.

Introduction

The combustion of fossil fuels not only provides power for society's development, but also releases large amounts of greenhouse gas, especially carbon dioxide (CO_2).[1–3] To mitigate human-induced climate change, conversion of CO_2 to valuable carbon-based fuels is deemed as an ideal technology to store renewable energy and alleviate the global warming issue.[4,5] Therefore, many catalytic methods were developed for the carbon dioxide reduction reaction (CRR) under ambient conditions, including thermal catalysis, electrocatalysis, and photocatalysis.[6–8] In comparison with electrochemical and thermal catalysis all needing external massive energy input, photocatalytic reduction of CO_2 on semiconductor materials is driven by solar electricity and water at room temperature.[9–11] On account of the inert nature of the CO_2 molecule, the CRR is a significantly challenging process.[12,13] In addition, owing to the product diversity, it is hard to acquire a pristine valuable chemical during the reduction process.[13–15] Therefore, it is urgent to find promising photocatalysts that hold excellent catalytic performance and product selectivity.[16,17]

In the literature, numerous photocatalysts have been extensively reported, including Zn,[18,19] noble metals,[20–22] heterostructures,[23,24] TiO_2,[14,25] MgO,[26] In_2O_3,[27] and CeO_2.[28,29] However, the low conversion efficiency hinders the commercial application of those photo-materials in the CRR.[30,31] Ideally, the photocatalyst should have high light utilization and low electron–hole carrier recombination rate.[32,33] Among those candidate materials, CeO_2-based photocatalysts take advantage of thermal stability, cheap price, good redox ability, and high oxygen storage capacity.[34–36] Methanol (CH_3OH) was successfully synthesized on CeO_2 nanoparticles by introducing oxygen vacancies under the assistance of sunlight.[37] In addition, CO_2 was converted to dimethyl carbonate on the pure CeO_2 surface with surface vacancy clusters. It is claimed that frustrated Lewis pairs benefit the C–C coupling and stabilize the key intermediates.[38] Unfortunately, narrow light absorption and product diversity make pure materials far away from the industrial requirement. To improve the reaction rate of the CRR and light absorption efficiency, a dopant is introduced into CeO_2, achieving excellent catalytic performance, because it enhances the ionic conductivity, and manipulates the electronic structure and oxygen vacancy formation. Consequently, many individual dopants were investigated such as Ga, Sm, La, Bi, and Pr.[39–42] Importantly, compressive strain engineering also has been widely conducted to tune the electronic structure and decrease the recombination rate of electron–hole pairs.[7,40]

In this work, we chose the bismuth (Bi) atom as the dopant for improving the CRR catalytic performance on the CeO_2 (111). It has two reasons: first, the ionic conductivity and band gap of

[a]*Liaoning Provincial Key Laboratory of Metallurgical Resources Circulation Science, Northeastern University, Shenyang, 110819, P. R. China*

[b]*State Key Laboratory of Catalysis, Dalian Institute of Chemical Physics, Chinese Academy of Sciences, Dalian 116023, China. E-mail: cwliu@dicp.ac.cn*

[c]*Sichuan Anxinda Rare Earth Technology Co. Ltd, Ya'an, 625400, P. R. China*

[d]*Naval Aviation University Qingdao Campus, Qingdao, Shandong 266041, China*

[e]*School of Materials and Energy, University of Electronic Science and Technology of China, Chengdu 610054, P. R. China. E-mail: wenjuntang9711@gmail.com*

† Electronic supplementary information (ESI) available. See DOI: https://doi.org/10.1039/d3se01680c

CeO_2 are significantly improved by the addition of Bi^{3+}/Bi^{5+}. Second, the Bi atom has been confirmed as a formate-producing material with high product selectivity. Then, we compare the CRR activity on oxygen vacancies (V_O), substituting one lattice Ce (S_{Bi}) with an oxygen vacancy (V_{Bi}), and substituting two lattice Ce atoms with an oxygen vacancy (V_{Bis}), by using density functional theory corrected for on-site coulombic interactions (DFT + U, $U_f = 4$). More importantly, the CRR activity of promising photocatalysts is improved by introducing the compressive strain. This exploration offers insights into the strain engineering influence on the turnover frequency (TOF) by tuning the intermediates and kinetic barrier.

Computational methods

In this work, all the computations about those structures and energies were based on the standard density functional theory using the Vienna *ab initio* Simulation Package (6.3.2 VASP).[43] The electron-exchange correlation functional was treated through the generalized gradient approximation (GGA) with the revised Perdew–Burke–Ernzerhof (RPBE), due to the functional giving more suitable results for adsorbed intermediates.[44,45] The 500 eV energy cutoff was adopted and the Brillouin zone was sampled with $3 \times 3 \times 1$ k-points using the Monkhorst–Pack scheme grid for geometry optimization and self-consistent calculations. We adopted $9 \times 9 \times 1$ k-points for band gap and density of state (DOS) calculations. A Hubbard U term was used to describe the electron localization on the 4f shells of the Ce atom.[41] A vacuum space exceeding 20 Å was employed to avoid the interaction between two periodic units. The atomic position was fully relaxed until the maximum force on each atom was less than -0.01 eV $Å^{-1}$ and 10^{-5} eV. Thermal and zero-point energy (ZPE) corrections were calculated over Γ points. The van der Waals interaction has been considered using the DFT-D_3 scheme.[46,47] The free energy of adsorption of A species (ΔG_{A*}) can be calculated by

$$\Delta G_{A*} = \Delta E_{A*} + \Delta E_{ZPE} - T\Delta S_{A*}$$

where the ΔE_{A*} is the energy needed to increase the coverage by one A species. And in the individual catalytic process, the ΔE_{A*} is described as

$$\Delta E_{A*} = E_{A*} - E_{cat} - E_A$$

And the ΔE_{ZPE} is the zero-point energy difference between the adsorbed and the free state, and ΔS_{A*} is their entropy difference. The energetic span approximation is applied to calculate the TOF:[48]

$$\mathrm{TOF} = \frac{k_B T}{h} e^{\delta E / k_B T}$$

In this approximation, the free energies of the TOF-determining transition state (G_{TDTS}) and TOF-determining intermediate state (G_{TDI}), and the free energy of the reaction (ΔG_r) define δE:

$$\delta E = \begin{cases} G_{TDTS} - G_{TDI}, & \text{if TDTS appears after TDI} \\ G_{TDTS} - G_{TDI} + \Delta G_r, & \text{if TDTS appears before TDI} \end{cases}$$

To approximate the energetic span, we calculate the thermodynamic energetic span as $\delta E' = G_{HI} - G_{LI} + \Delta G_r$, where G_{HI} is the free energy of the reaction intermediate with the highest free energy and G_{LI} is the free energy of the reaction intermediate with the lowest free energy.

Results and discussion

The optimized configurations of the above four potential models are shown in Fig. S1,† corresponding to the side and top views, respectively. As shown in Fig. S1b,† the equilibrium structures of S_{Bi} retain perfect $CeO_2(111)$ structural characteristics, indicating that the Bi atom has a similar size to the Ce. Fig. 1a shows the different distributions of Bi doping with or without oxygen vacancies in the $CeO_2(111)$. Initially, the thermodynamic stability of these concept photocatalysts is evaluated by the formation energy, as shown in Fig. 1b. The formation energy of simple substitution (S_{Bi}) and oxygen vacancies (V_O) is positive, especially the value of V_O is up to 1.85 eV. Therefore, the V_O structure is very unstable under mild conditions. Interestingly, the formation energy changes to negative when introducing the Bi dopant into the pure material with one oxygen vacancy. The value decreases with the increase of dopants, and the formation energy of V_{Bis} almost closes to zero (-0.03 eV). As described by the energy, those concept-catalysts could be easily synthesized by experimental methods.[49,50] Then the CRR performance of S_{Bi}, V_{Bi}, and V_{Bis} is further evaluated in the following part. By comparing the work function (Fig. 1c) and optimized structures of these surfaces, the following results can be deduced: (1) the Bi-dopant improves the ability of electromigration; (2) V_{Bi} has the lowest work function. Then the potentially active surface is further analyzed by electron localization function and Bader charge studies (Fig. 1d–f). Every oxygen atom receives about $1.15|e|$ electron from the Ce atom, losing about $2.30|e|$. While the Ce and O atoms still keep the same number of electron exchanges in the S_{Bi} structure. In other words, the Bi transfers the same number of electrons ($2.30|e|$) to the oxygen atom. The Bader charge of the O atom still keeps the same value after introducing the oxygen vacancy, and electron transfer of Bi and Ce is decreased. In addition, some pioneering studies confirmed that oxygen vacancies in the CeO_2 surface benefit the frustrated Lewis pair (FLP) catalysts formed.[38,51,52] The local electron density and the steric electron transferred are redistributed in the surface defects in CeO_2. The Bi–O–Ce structure not only narrows the band gap of CeO_2, but also enhances the rapid transfer of electrons between the reaction intermediates and the catalyst.

As we know, the CRR is a complicated process, and many products will occur on the different catalysts, such as CO, CH_4, HCOOH, and C_{2+}. Various efforts confirm the first reduction intermediate is key for the selectivity of CO_2 reduction.[53] For example, the *OCHO is considered as a feasible indicator for

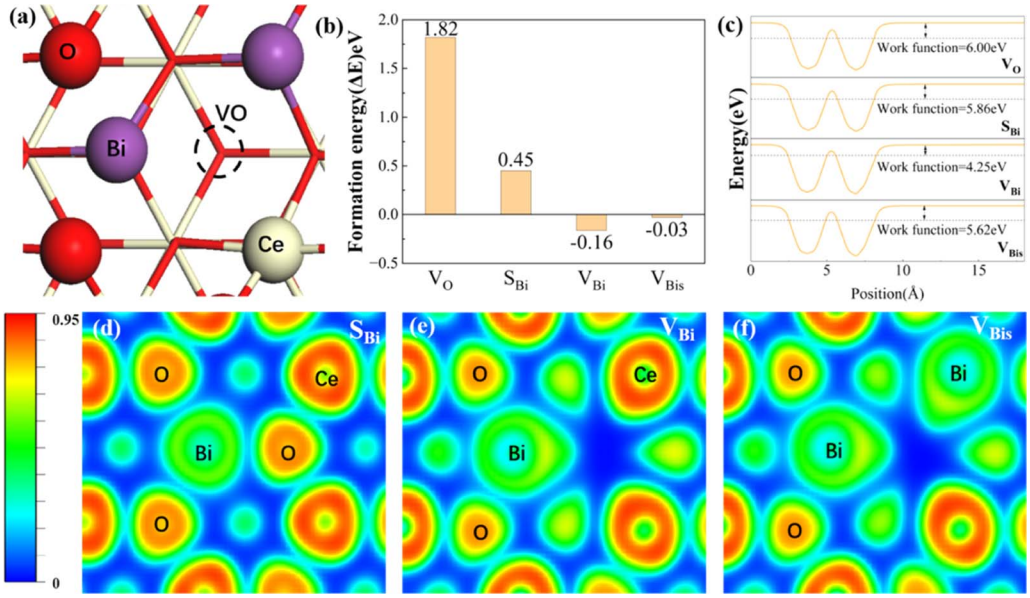

Fig. 1 (a) Configuration of four concept structures in CeO_2 (111). The formation energy (b), work function (c), and electron localization function (d–f) of the above four materials. White, red, and purple represent Ce, O, and Bi, respectively.

HCOOH, however, the adsorption energy of *CO has a high relationship with the C_{2+} products. In the initial adsorption process, the distance between the CO_2 and active site is larger than 3.5 Å with a small energy input. In other words, the CO_2 molecule is adsorbed on the above three promising surfaces by physical adsorption. For the first reduction step (CO_2 → *COOH), the activation energy on the S_{Bi} needs about 2.22 eV, and the intermediate (*COOH) still lies in the vacuum space (Fig. S2†). Therefore, the structure is not fit for the CRR under ambient conditions, while two intermediates, including *COOH and *OCHO, are produced on the V_{Bi} model in the first reduction step. Interestingly, the catalytically active site is the Ce atom instead of the Bi site. The first reduction step with ΔG values being 0.89 eV and −0.69 eV for *COOH and *OCHO intermediates, respectively, indicates that the *OCHO configuration should dominate the reduction process. Specifically, the bond length of C–O is up to 1.28 Å (1.21 Å for free gas) indicating that the Ce remarkably injects electrons into the intermediate. Bader charge analyses indicate that the *COOH and *OCHO receive 0.68 and 0.76|*e*| from the substrate, respectively, in which the Ce atom transfers the most electrons to intermediates. In the following hydrogenation step, the reaction energy

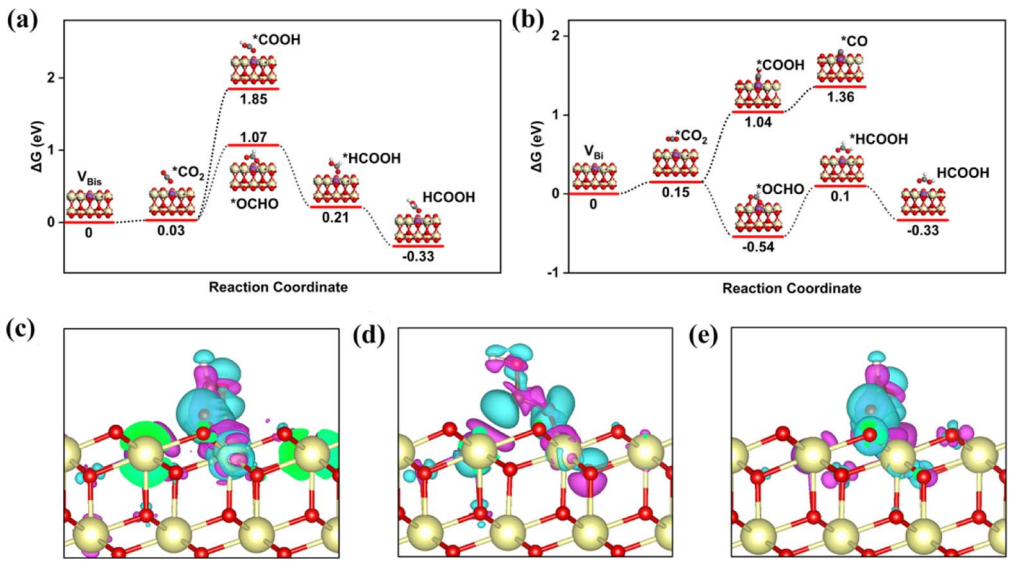

Fig. 2 Free energy profile for the CRR on V_{Bi} (a) and V_{Bis} (b) with various intermediates. Electron density difference plots for *OCHO (c), *COOH (d) on V_{Bi}, and *COOH (d) on V_{Bis}. The isosurface value was set to 0.003 e $Å^{-3}$. The charge accumulation and loss are shown in the cyan and pink regions, respectively. Black represents C.

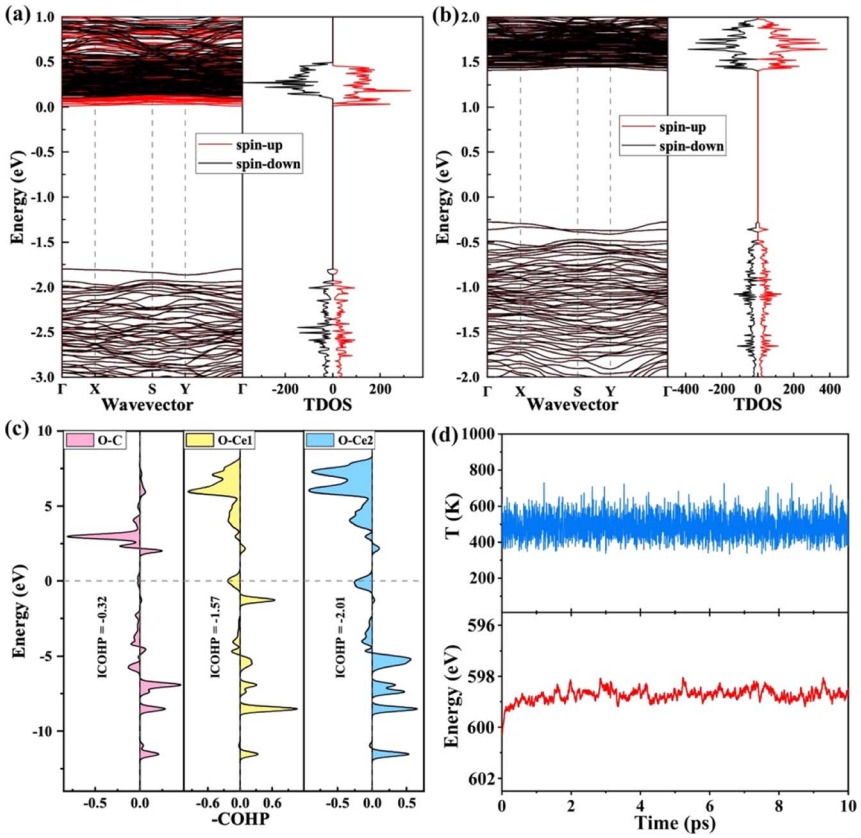

Fig. 3 Calculated electronic structures of V_{Bi} (a) and V_{Bis} (b). The Fermi energy is set as zero. (c) Projected crystal orbital Hamilton population (pCOHP) between O–C, O1–Ce1 and O2–Ce2. (d) Fluctuation of temperature and energy *versus* time (10 ps).

still needs about 0.31 eV, and CO is provided during the step. Subsequently, the CO will be easily released with an exothermic process. During the *OCHO → *HCOOH step, the reaction is endothermic in the energy profile by 0.64 in Fig. 2b. The formic acid is spontaneously released from the V_{Bi} surface with a small energy release (0.43 eV). No matter what, for the two hydrogenation pathways of CO_2, *OCHO exhibits a stronger thermodynamic tendency compared to *COOH, and particularly noteworthy is that the further hydrogenation of *OCHO in the V_{Bi} structure reaches a ΔG of −0.86 eV, indicating that this pathway is thermodynamically the most favourable.

The isosurfaces of the charge density of *OCHO and *COOH configurations for V_{Bi} have been investigated in Fig. 2c and d, which indicate that *OCHO is the favorable product from the more charge transfer from the substrate to *OCHO. Therefore, the water-solvation mechanism is the main reaction pathway. Following this route, the CRR performance of the V_{Bis} catalyst is estimated. The *COOH intermediate cannot be adsorbed on the V_{Bis} surface with an endothermic reaction process. But this reaction pathway is not eligible for CO_2 activation due to the requirement of a heavy energy input (1.82 eV). For the *OCHO intermediate, the C–O bond length is up to 1.26 Å from 1.21 Å, indicating that the C–O is activated slightly in this process. And the input activation energy in this way is about 1.04 eV. Then the HCOOH is released by two exothermic processes. And the *OCHO chemisorption on V_{Bis} is presented in Fig. 2e, along with the corresponding charge density differences. The charge accumulation and Bader charge studies of *OCHO (0.66|e|) indicate that the intermediate gains some electrons from the substrate. From the above results, four features are achieved: (a) a slight energy requirement for CO_2 physical adsorption is observed on the catalyst surface; (b) the catalytic site is the Ce atom, while the Bi atom benefits the oxygen vacancy formed; (c) HCOOH is the preferred product; (d) the V_{Bi} structure not only holds the lowest work function, but also presents the best catalytic performance for the CRR (ΔG_{max} = 0.64 eV).

Researchers found that the oxygen vacancy formation energy and bandgap for the Bi-doped CeO_2 are reduced by electronic and structural modification, improving the redox properties.[54,55] In addition, the Bi-doped CeO_2 with one oxygen vacancy remarkably benefits the photogenerated electron–hole pair separation, indicating that more electrons are produced during light irradiation. In order to deeply study the role of the Bi atom on the CeO_2 (111) structure for effective CRR, the electronic band structure is calculated for the bulk-CeO_2, V_{Bi}, and V_{Bis}, as shown in Fig. 3a and b. The bandgaps for the three structures are 1.98, 1.76, and 1.85 eV, respectively, by using RPBE + U. It can be seen that the value of the bulk phase is consistent with the previously reported values. The neutral oxygen vacancy with Bi-doping leaves two electrons to the adjacent Ce atoms, reducing the valency from Ce^{4+} to Ce^{3+}. Moreover, the dopant presents Bi^{5+} under this condition, which makes the

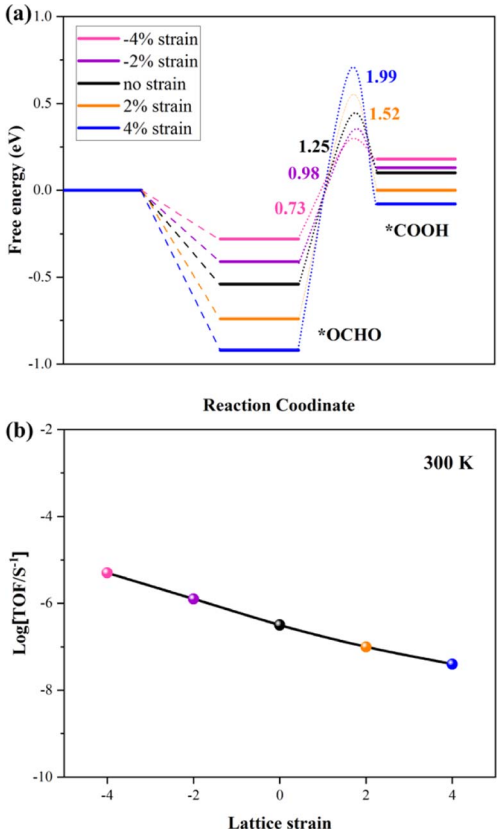

Fig. 4 (a) Kinetic barriers for *OCHO to *COOH on the V_{Bi} structure with different strains. (b) TOF of the CRR *versus* different strains under 300 K.

surrounding Ce atoms receive more electrons. As is known, O_{2P} presents the valence band (VB), and the metal atom donates the conduction band (CB). In addition, the oxygen vacancy states provide the occupied CB states, confirming the presence of Ce^{3+} ions. Moreover, the electronic band structure of CeO_2 is changed by the d orbital of the Bi atom, and a new band between the VB and CB is contributed. The reduced bandgap indicates that the conductive properties of Bi-doped CeO_2 are changed, because the Bi improves ionic conductivity. The high ionic conductivity also further decreases the formation energy of oxygen vacancies. Amazingly, the V_{Bi} structure has the relatively lowest bandgap, which is consistent with the work function result, overall, the V_{Bi} structure is confirmed as an excellent photocatalyst for the CRR.

Generally, the electron transfer between the active site and intermediate is essential for the reduction process. In other words, the electron-accumulated catalytic site can transfer more electrons to the *OCHO on the V_{Bi} structure. To support this claim, the projected crystal orbital Hamilton populations (pCOHP) of O–C, O1–Ce1, and O2–Ce2 have been summarized in Fig. 3c. Ce1 and Ce2 (yellow and blue lines) dominate all the valence bond states, which all agree with the Ce–O bonding nature. The bond O2–Ce2 is slightly stronger than the O1–Ce1 below the Fermi level. The conclusion is verified by the Bader charge result, according to that the O1 and O2 gain 1.14 and 1.23|*e*| from the catalytic sites, respectively. In brief, Bi–O–Ce structure coexistence can tune the electron distribution and build a synergetic effect mechanism for the CRR. To further guide the experimental work, the stability of the V_{Bi} structure is studied by *Ab Initio* Molecular Dynamics simulation (AIMD) under 500 K, as shown in Fig. 3d. The model still keeps the same structure under this temperature, indicating excellent thermodynamic stability under experimental conditions. The fluctuation temperature and energy of the promising material are further investigated about 10 ps. The plot shows that the fluctuation of the two features is close to the equilibrium state. Then, it can be claimed that the potential structure not only possesses excellent photocatalytic activity for the CRR under visible light, but also presents outstanding stability under the experimental reaction conditions.

Many theoretical and experimental studies confirmed that the strain plays an important role in modulating the adsorption energy of the intermediate and tuning the kinetic barriers. The first reduction step (*OCHO → *HCOOH) is the rate-determining step (RDS) in this work. So, the kinetic barrier of this step is investigated by using the Langmuir–Hinshelwood mechanism, as shown in Fig. 4a. The thermodynamic barrier (E_a) for hydrogenation along each reaction pathway enhances with increasing tensile strain, while the adsorption energy of intermediates reduces with increasing compressive strain. The adsorption energies of the two intermediates have a scaling relation with applied compressive strain, indicating that strain-induced stronger adsorption can stabilize transition states and reduce the kinetic barrier, which is critical to achieving large reaction rates. The result shows that the *OCHO and transition state (*OCHO → *HCOOH) have been considered as the TDI (TOF-determining intermediate) and TDTS (TOF-determining transition state), respectively. Finally, the Energetic Span Model is employed to calculate the turnover frequency (TOF) under 300 K, and the calculation results are summarized in Fig. 4b. The profile indicates that the potential catalyst presents the best CRR catalytic performance under comprehensive strain. Our conclusion offers a direct relationship between kinetic parameters and experimentally accessible descriptors.

Conclusions

In summary, by performing first-principles calculations, a new single Bi atom doped CeO_2 catalyst for the conversion of CO_2 to HCOOH is proposed under ambient conditions. By comparing the reaction activity and product selectivity, the V_{Bi} structure is considered an outstanding photocatalyst for the CRR under ambient conditions. While the Ti with one oxygen vacancy is the main catalytic site, the Bi-dopant benefits the vacancy formed and rearranges the electrons on the surface. The main product is formic acid, having a relatively low thermodynamics (0.64 eV). Furthermore, the AIMD results show that the model expresses good kinetic stability with experimental methods. With applying compressive strain, the adsorption energy of the intermediate and the kinetic barrier of RDS all decreased. In other words, the catalytic activity increases with an increase in the compressive stain. TOF achieves the maximum value under

4% compressive strain under 300 K. These results provide novel routes for the rational design and development of excellent CeO_2-based photocatalysts toward carbon reduction.

Conflicts of interest

There are no conflicts to declare.

Acknowledgements

We acknowledge the Foundation of China's National Key R&D Programme (grant no. 2023YFB3810600) and Basic Scientific Research Foundation of Central College (grant no. 2125032). The authors also acknowledge funding of Technology and Innovation (grant no. KJ2021-01), which is supported by Ya'an City.

References

1 C. Liu, A. Tian, Q. Li, T. Wang, G. Qin, S. Li and C. Sun, *Adv. Funct. Mater.*, 2023, **33**, 2210759.
2 Q. Hao, C. Liu, G. Jia, Y. Wang, H. Arandiyan, W. Wei and B.-J. Ni, *Mater. Horiz.*, 2020, **7**, 1014–1029.
3 H. Yuan, J.-H. Mei, Y.-N. Gong, D.-C. Zhong and T.-B. Lu, *Tungsten*, 2023, DOI: **10.1007/s42864-023-00208-2**.
4 Y. Yu, D. Wang, Y. Hong, T. Zhang, C. Liu, J. Chen, G. Qin and S. Li, *Chem. Commun.*, 2022, **58**, 11163–11166.
5 Q. Wu, C. Liu, X. Su, Q. Yang, X. Wu, H. Zou, B. Long, X. Fan, Y. Liao, L. Duan, Z. Quan and S. Luo, *ACS Nano*, 2023, **17**, 402–410.
6 S. Das, J. Pérez-Ramírez, J. Gong, N. Dewangan, K. Hidajat, B. C. Gates and S. Kawi, *Chem. Soc. Rev.*, 2020, **49**, 2937–3004.
7 C. Liu, T. Wang, D. Hao, Q. Li, S. Li and C. Sun, *J. Mater. Sci. Technol.*, 2022, **110**, 96–102.
8 C. L. Hugelshofer, A. Borgschulte, E. Callini, S. K. Matam, J. Gehrig, D. T. Hog and A. Züttel, *J. Phys. Chem. C*, 2014, **118**, 15940–15945.
9 E. V. Kondratenko, G. Mul, J. Baltrusaitis, G. O. Larrazábal and J. Pérez-Ramírez, *Energy Environ. Sci.*, 2013, **6**, 3112–3135.
10 C. Liu, D. Hao, J. Ye, S. Ye, F. Zhou, H. Xie, G. Qin, J. Xu, J. Liu, S. Li and C. Sun, *Adv. Energy Mater.*, 2023, **13**, 2204126.
11 Ž. Kovačič, B. Likozar and M. Huš, *ACS Catal.*, 2020, **10**, 14984–15007.
12 C. Costentin, M. Robert and J.-M. Savéant, *Chem. Soc. Rev.*, 2013, **42**, 2423–2436.
13 Y. Jiao, Y. Zheng, P. Chen, M. Jaroniec and S.-Z. Qiao, *J. Am. Chem. Soc.*, 2017, **139**, 18093–18100.
14 J.-Y. Liu, X.-Q. Gong and A. N. Alexandrova, *J. Phys. Chem. C*, 2019, **123**, 3505–3511.
15 Y. Chen, G. Jia, Y. Hu, G. Fan, Y. H. Tsang, Z. Li and Z. Zou, *Sustainable Energy Fuels*, 2017, **1**, 1875–1898.
16 Y. Miao, Y. Zhao, S. Zhang, R. Shi and T. Zhang, *Adv. Mater.*, 2022, **34**, 2200868.
17 B. Su, M. Zheng, W. Lin, X. F. Lu, D. Luan, S. Wang and X. W. Lou, *Adv. Energy Mater.*, 2023, **13**, 2203290.
18 Y. Zhao, G. Chen, T. Bian, C. Zhou, G. I. N. Waterhouse, L.-Z. Wu, C.-H. Tung, L. J. Smith, D. O'Hare and T. Zhang, *Adv. Mater.*, 2015, **27**, 7824–7831.
19 X. Xiong, Y. Zhao, R. Shi, W. Yin, Y. Zhao, G. I. N. Waterhouse and T. Zhang, *Sci. Bull.*, 2020, **65**, 987–994.
20 Q. L. Cheng Luo, B. Cheng, B. Zhu and L. Wang, *Acta Phys.-Chim. Sin.*, 2023, **39**, 2212026.
21 G. Huang, Q. Niu, J. Zhang, H. Huang, Q. Chen, J. Bi and L. Wu, *Chem. Eng. J.*, 2022, **427**, 131018.
22 B. Su, Y. Kong, S. Wang, S. Zuo, W. Lin, Y. Fang, Y. Hou, G. Zhang, H. Zhang and X. Wang, *J. Am. Chem. Soc.*, 2023, **145**, 27415–27423.
23 M. Hao, D. Wei and Z. Li, *Energy Fuels*, 2022, **36**, 11524–11531.
24 L. Wang, X. Zhao, D. Lv, C. Liu, W. Lai, C. Sun, Z. Su, X. Xu, W. Hao, S. X. Dou and Y. Du, *Adv. Mater.*, 2020, **32**, 2004311.
25 C. Liu, A. Tian, H. Yang and X. Xue, *Mater. Lett.*, 2013, **106**, 1–4.
26 Y. Kohno, H. Ishikawa, T. Tanaka, T. Funabiki and S. Yoshida, *Phys. Chem. Chem. Phys.*, 2001, **3**, 1108–1113.
27 K. K. Ghuman, T. E. Wood, L. B. Hoch, C. A. Mims, G. A. Ozin and C. V. Singh, *Phys. Chem. Chem. Phys.*, 2015, **17**, 14623–14635.
28 K. R. Hahn, M. Iannuzzi, A. P. Seitsonen and J. Hutter, *J. Phys. Chem. C*, 2013, **117**, 1701–1711.
29 A. Tian, T. Ma, X. Shi, D. Wang, W. Wu, C. Liu and W. Pei, *Coatings*, 2021, **11**, 1095.
30 M. Kanemoto, T. Shiragami, C. Pac and S. Yanagida, *J. Phys. Chem.*, 1992, **96**, 3521–3526.
31 Y. S. Chaudhary, T. W. Woolerton, C. S. Allen, J. H. Warner, E. Pierce, S. W. Ragsdale and F. A. Armstrong, *Chem. Commun.*, 2012, **48**, 58–60.
32 K. Li, B. Peng and T. Peng, *ACS Catal.*, 2016, **6**, 7485–7527.
33 W. Tu, Y. Zhou and Z. Zou, *Adv. Mater.*, 2014, **26**, 4607–4626.
34 Y.-Q. Su, Y.-Y. Qin, T. Wu and D.-Y. Wu, *J. Catal.*, 2022, **407**, 353–363.
35 J. Cai, D. Li, L. Jiang, J. Yuan, Z. Li and K. Li, *Energy Fuels*, 2023, **37**, 4878–4897.
36 T. Wu, T. Vegge and H. Anton Hansen, *J. Catal.*, 2023, **420**, 1–8.
37 A. Hezam, K. Namratha, Q. A. Drmosh, D. Ponnamma, J. Wang, S. Prasad, M. Ahamed, C. Cheng and K. Byrappa, *ACS Appl. Nano Mater.*, 2020, **3**, 138–148.
38 L. Li, W. Liu, R. Chen, S. Shang, X. Zhang, H. Wang, H. Zhang, B. Ye and Y. Xie, *Angew. Chem., Int. Ed.*, 2022, **61**, e202214490.
39 A. Shahzadi, S. Moeen, A. D. Khan, A. Haider, J. Haider, A. Ul-Hamid, W. Nabgan, I. Shahzadi, M. Ikram and A. Al-Shanini, *ACS Omega*, 2023, **8**, 8605–8616.
40 S. Tang, L. Xu, B. Peng, F. Xiong, T. Chen, X. Luo, X. Huang, H. Li, J. Zeng, Z. Ma and L.-L. Wang, *Appl. Surf. Sci.*, 2022, **575**, 151655.
41 T. Wu, T. Vegge and H. A. Hansen, *J. Catal.*, 2021, **402**, 310–314.
42 T. Wu, Q. Deng, H. A. Hansen and T. Vegge, *J. Phys. Chem. C*, 2019, **123**, 5507–5517.

43 G. Kresse and D. Joubert, *Phys. Rev. B: Condens. Matter Mater. Phys.*, 1999, **59**, 1758–1775.
44 J. P. Perdew, K. Burke and M. Ernzerhof, *Phys. Rev. Lett.*, 1996, **77**, 3865–3868.
45 C. Liu, Q. Li, C. Wu, J. Zhang, Y. Jin, D. R. MacFarlane and C. Sun, *J. Am. Chem. Soc.*, 2019, **141**, 2884–2888.
46 L. M. Azofra, N. Li, D. R. MacFarlane and C. Sun, *Energy Environ. Sci.*, 2016, **9**, 2545–2549.
47 G. Mills, H. Jónsson and G. K. Schenter, *Surf. Sci.*, 1995, **324**, 305–337.
48 C. Liu, Q. Wang, J. Guo, T. Vegge, P. Chen and H. A. Hansen, *ACS Catal.*, 2022, **12**, 4194–4202.
49 C. Santra, A. Auroux and B. Chowdhury, *RSC Adv.*, 2016, **6**, 45330–45342.
50 B. Cui, Y. Li, S. Li, Y. Xia, Z. Zheng and Y.-Q. Liu, *Energy Fuels*, 2020, **34**, 9932–9939.
51 J. C. M. Pereira, M. Sajid, G. Kehr, A. M. Wright, B. Schirmer, Z.-W. Qu, S. Grimme, G. Erker and P. C. Ford, *J. Am. Chem. Soc.*, 2014, **136**, 513–519.
52 D. W. Stephan, *Acc. Chem. Res.*, 2015, **48**, 306–316.
53 X. Zhi, Y. Jiao, Y. Zheng, A. Vasileff and S.-Z. Qiao, *Nano Energy*, 2020, **71**, 104601.
54 D. A. Andersson, S. I. Simak, B. Johansson, I. A. Abrikosov and N. V. Skorodumova, *Phys. Rev. B: Condens. Matter Mater. Phys.*, 2007, **75**, 035109.
55 Y. Tang, H. Zhang, L. Cui, C. Ouyang, S. Shi, W. Tang, H. Li, J.-S. Lee and L. Chen, *Phys. Rev. B: Condens. Matter Mater. Phys.*, 2010, **82**, 125104.